



HAL
open science

Development of decision support tools by model order reduction for active endovascular navigation

Arif Badrou, Arnaud Duval, Jérôme Szewczyk, Raphaël Blanc, Nicolas Tardif, Nahiene Hamila, Anthony Gravouil, Aline Bel-Brunon

► To cite this version:

Arif Badrou, Arnaud Duval, Jérôme Szewczyk, Raphaël Blanc, Nicolas Tardif, et al.. Development of decision support tools by model order reduction for active endovascular navigation. 2022. hal-03858565v3

HAL Id: hal-03858565

<https://hal.science/hal-03858565v3>

Preprint submitted on 4 Jan 2024

HAL is a multi-disciplinary open access archive for the deposit and dissemination of scientific research documents, whether they are published or not. The documents may come from teaching and research institutions in France or abroad, or from public or private research centers.

L'archive ouverte pluridisciplinaire **HAL**, est destinée au dépôt et à la diffusion de documents scientifiques de niveau recherche, publiés ou non, émanant des établissements d'enseignement et de recherche français ou étrangers, des laboratoires publics ou privés.



Distributed under a Creative Commons Attribution 4.0 International License

Development of decision support tools by model order reduction for active endovascular navigation

Arif Badrou¹,  Arnaud Duval¹, Jérôme Szewczyk^{2,3},  Raphaël Blanc^{2,4},  Nicolas Tardif¹,  Nahiène Hamila⁵,  Anthony Gravouil¹, and  Aline Bel-Brunon¹

¹ Univ Lyon, INSA Lyon, CNRS, LaMCoS, UMR5259, 69621 Villeurbanne, France

² BaseCamp Vascular (BCV), 75005 Paris, France

³ Sorbonne Université, CNRS, INSERM, Institut des Systèmes Intelligents et de Robotique, ISIR, ISIR - AGATHE, F-75005 Paris, France

⁴ Department of Interventional Neuroradiology, Fondation Rothschild Hospital, Paris, France

⁵ Ecole Nationale d'Ingénieurs de Brest, ENIB, UMR CNRS 6027, IRDL, F-29200, Brest, France

1 Endovascular therapies consist in treating vascular pathologies mini-invasively by inserting long tools
2 towards the area to treat. However, some trajectories are so-called complex (e.g. Supra-Aortic Trunks
3 (SATs)). In order to facilitate the access to complex targets by catheterization, an active guidewire made of
4 Shape Memory Alloy has been developed. Our study focuses on the navigation of this device and associated
5 catheters towards neurovascular targets through the left carotid artery. In a previous study, a finite element
6 model was developed to simulate the navigation of the active guidewire and catheters from the aortic arch
7 to the hooking of the left carotid artery of patient-specific aortas. However, numerical simulations are
8 time-consuming and cannot be used directly in the clinic routine to provide navigation assistance. We
9 present in this study the development of numerical charts aiming to provide a real-time computation,
10 based on high-fidelity FE simulations, of: 1. the behaviour of the active guidewire; 2. the navigation of the
11 active guidewire and associated catheters within a given anatomy for specific guidewire and navigation
12 parameters. These charts are developed using the High Order Proper Generalized Decomposition (HOPGD)
13 method and demonstrate their ability to provide an accurate real-time response from a limited number of
14 preliminary high-fidelity computations.

15 **Keywords** Model Order Reduction, Numerical chart, Endovascular, Catheters, Guidewire, Aorta

17 **0.1 Introduction**

18 Endovascular therapies have grown significantly in the recent years. It is estimated that in 2026,
19 80% of cardiovascular problems will be treated by endovascular therapies (Veith 2016). The
20 first step to treat endovascular pathologies is to reach the pathologies area. However, clinicians
21 may be confronted to so-called complex pathways (e.g. renal arteries or Supra-Aortic Trunks
22 (SATs)). It is estimated that 20% endovascular therapies present these complexities which may
23 jeopardize the intervention (Madhwal et al. 2008). In order to facilitate the access to complex
24 targets through catheterization, the French company BaseCamp Vascular (BCV) developed an
25 active guidewire made of Shape Memory Alloy, which distal tip can bend under an electric

26 impulse. This guidewire can include several active modules; for instance for 2 modules placed in
27 opposite directions, the guidewire tip can take an S-shape.

28 Our work focuses on the access to neurovascular pathologies through the left carotid artery
29 using the active guidewire and associated catheters. Access to cerebral targets is facilitated
30 using the active guidewire but two challenges remain for a given anatomy: (i) to optimize the
31 design of the active guidewire by assessing the number of required actuators and their respective
32 curvature and (ii) to propose navigation sequences maximizing the chances of reaching the target.
33 A Finite Element (FE) model was developed to simulate the navigation of the active guidewire and
34 catheters from the aortic arch to the left carotid artery in patient-specific aortas (Badrou, Tardif,
35 Chaudet, et al. 2022). The numerical model offers the possibility to test particular guidewire
36 configurations and navigation sequences.

37 However, numerical simulations are time-consuming and cannot be used directly in clinical
38 routine to provide navigation assistance. An alternative is to develop numerical charts to explore
39 in a continuous way a wide range of parameters for a limited computational cost.

40 Numerical charts are built using Model Order Reduction (MOR) techniques. Two families of
41 MOR are commonly used. The methods known as POD (Proper Orthogonal Decomposition)
42 require calculations in an offline phase (learning phase), further allowing reduction and online
43 resolution in the reduced base (in real-time). In biomechanics and in particular for vascular
44 problems, POD was used for example to process hemodynamic data (Kefayati et al. 2013; Janiga
45 2019; Darwish et al. 2021) or to reduce the computational time of complex models (Rama et al.
46 2016). The methods known as PGD (Proper Generalized Decomposition) based on the separation
47 of variables, do not require upstream calculations. In particular, PGD is used for inverse problem
48 solving: in Barone et al. (2020), PGD was used to speed up the process of identifying conductivities
49 of heart tissue. Other works have used PGD for computational surgery, Quesada, González,
50 et al. (2016); Quesada, Alfaro, et al. (2018); Niroomandi et al. (2013) for example. One of the
51 limitations of POD is that it is not adapted to non-linear problems (large strains in particular) and
52 that the enrichment of the reduced bases can quickly become expensive for high dimensional
53 problems and/or with relatively large parameter intervals. By considering uniform grids, the
54 number of snapshots is exponential. For example, for a uniform grid of snapshots in a space of 8
55 parameters with 10 values to be considered in each direction, 10^8 finite element calculations
56 would be required. We then speak of *curse of dimensionality*. PGD allows to overcome this
57 problem since no snapshot is required. However, it remains an intrusive method and is therefore
58 not adapted to the use of commercial softwares. The method used in the present study is HOPGD
59 (High Order Proper Generalized Decomposition) (Modesto et al. 2015). It is an a posteriori

60 definition of PGD and has been used to produce 10-dimensional (10D) numerical charts in the
61 context of real-time numerical simulation of welding processes (Lu et al. 2018b). We aim to build
62 numerical charts based on our reference FE navigation model, to efficiently answer specific
63 questions regarding device design and navigation sequences.

64 We first recall the main features of the high-fidelity numerical models used in this study,
65 namely the guidewire model and the active endovascular navigation model. Then, HOPGD is
66 briefly presented and the methods for the development of numerical charts are detailed. Proofs of
67 concept of such charts ,developed to answer specific questions associated to endovascular active
68 navigation, are presented. The results are finally discussed in a last part.

69 **1 Methods**

70 **1.1 High fidelity models**

71 In this section, we present the high-fidelity models used to develop the numerical charts: first the
72 active guidewire model and second the navigation model.

73 **1.1.1 Active guidewire**

74 **1.1.1.1 Structure**

75 The active guidewire is composed of a long shaft made of steel. At its extremity, a blade is
76 attached and Nitinol wires are positioned on both sides of the blade and connected to electric
77 wires. A handle allows to send an electric impulse to the Nitinol wires and by shape memory
78 effect, the wires shrink causing the blade to bend (Lagoudas 2008; Couture et al. 2017). When two
79 Nitinol wires are placed on each face of the blade, the distal tip of the active guidewire draws a
80 S-shape to facilitate the endovascular navigation (see Fig.1).

81 **1.1.1.2 Numerical model**

82 The model is built using Ls-Dyna (LSTC / ANSYS, USA). The active guidewire is simplified, as not
83 all elements from Fig.1 are included, and represented as a long shaft with the blade. The Nitinol
84 wires are placed on both sides of the blade and connected by rigid links (see Fig.2). The guidewire
85 is meshed with Hughes-Liu beam elements. The constitutive law to model the mechanical
86 behavior of the guidewire is hypoelastic and relates, in Eulerian form, the objective Jaumann
87 derivative of the Cauchy stress tensor σ to the strain rate tensor \mathbf{D} by the elasticity tensor \mathbf{C} such
88 that:

$$\sigma^{\nabla} = \mathbf{C} : \mathbf{D} \quad (1)$$

89 Tensor \mathbf{C} can be decomposed into a spherical part \mathbf{C}^{sph} and a deviatoric part \mathbf{C}^{dev} such that:

$$\mathbf{C} = 3K\mathbf{C}^{sph} + 2G\mathbf{C}^{dev} \quad (2)$$

90 with K the bulk modulus and G the shear modulus.

91 The mechanical properties of the various portions of the guidewire were characterized in
 92 [Badrou, Tardif, Even, et al. \(2022\)](#) and the Young's moduli of the main components are recalled in
 93 Fig.2 with a fixed Poisson's ratio of 0.3 The guidewire activation is simplified and produced by a
 94 displacement command as explained in [Badrou, Tardif, Chaudet, et al. \(2022\)](#).

95 **1.1.1.3 Simulation of the guidewire activation**

96 Simulation of the guidewire is useful for guidewire developers to understand the guidewire
 97 performance, related to the Nitinol wires characteristics. The shaft is embedded and a temperature
 98 control is applied to both moduli for activation. The computational time for such a simulation is
 99 about 5 minutes. The output data are the displacements in 3D of the guidewire distal parts nodes
 100 (73 mm blade of the active guide) at the end of the simulation.

101 **1.1.2 Endovascular navigation**

102 **1.1.2.1 Test bench**

103 The endovascular activation simulated in this work has been validated with respect to data
 104 acquired on a test bench including a phantom aorta (Fig.1). The simulation features aim to
 105 reproduce this configuration and the phenomena observed on this bench. The set-up is composed
 106 of a patient-specific aortic arch which can be changed and a fixed cylinder representing the
 107 descending aorta. The active guidewire is inserted and co-manipulated along with catheters.

108 **1.1.2.2 Endovascular navigation model**

109 The numerical model simulates the endovascular navigation of the active guidewire and
 110 associated catheters in the aorta test bench. The catheters and the aorta are meshed with
 111 Belytschko-Tsay shell elements. The mechanical properties of the tools are either hypoelastic
 112 (using Eq.1) or hypoviscoelastic depending on the different areas.

113 Fig.2 illustrates the assembly of the different tools (guidewire and catheters) navigating in a

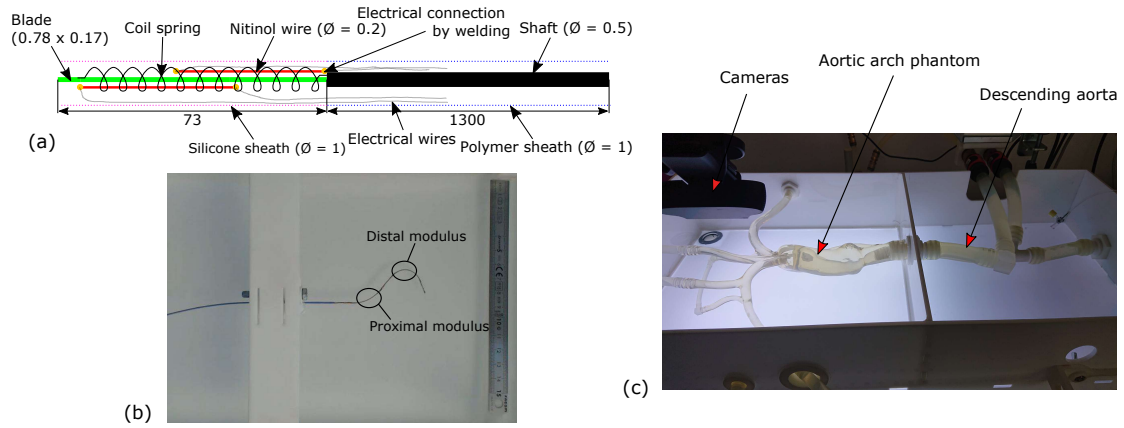


Figure 1: (a) Scheme of the active guidewire developed by BCV with two Nitinol wires placed on both sides of the blade and (b) its activation highlighting the proximal and the distal moduli. (c) Phantom aorta test bench used to test surgical tools in patient-specific aortas.

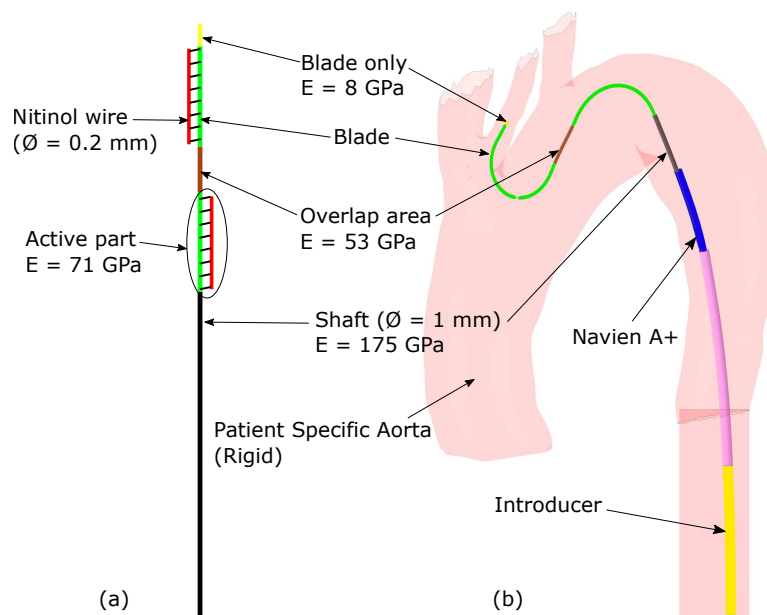


Figure 2: (a) Scheme of the simplified active guidewire. Each portion of the guidewire is defined by a colour and has its own mechanical properties. (b) Assembly of the different tools in a rigid aorta: the guidewire is activated drawing an S-shape to ease the navigation of the catheters. Once the guidewire reaches the desired artery, the Navien A+ catheter slides over it. The introducer (large catheter) is used to stabilize the navigation.

114 patient specific aorta considered as rigid. The dimensions as well as the material properties can be
 115 found in [Badrou, Tardif, Even, et al. \(2022\)](#). More details about the full navigation model are given
 116 in [Badrou, Tardif, Chaudet, et al. \(2022\)](#). The navigation model, involving guidewire activation
 117 but also tools translations and rotations within the aorta, was also validated as described in
 118 [Badrou, Tardif, Chaudet, et al. \(2022\)](#) by confronting experimental navigation in patient-specific
 119 aortas to simulated ones.

120 The model is able to reproduce the main movements and phenomena occurring in active
 121 navigation: translations of the guidewire and the catheter, rotations of the guidewire and
 122 particular effects such as the snapping (Fig.3). Navigation sequences will be detailed later.

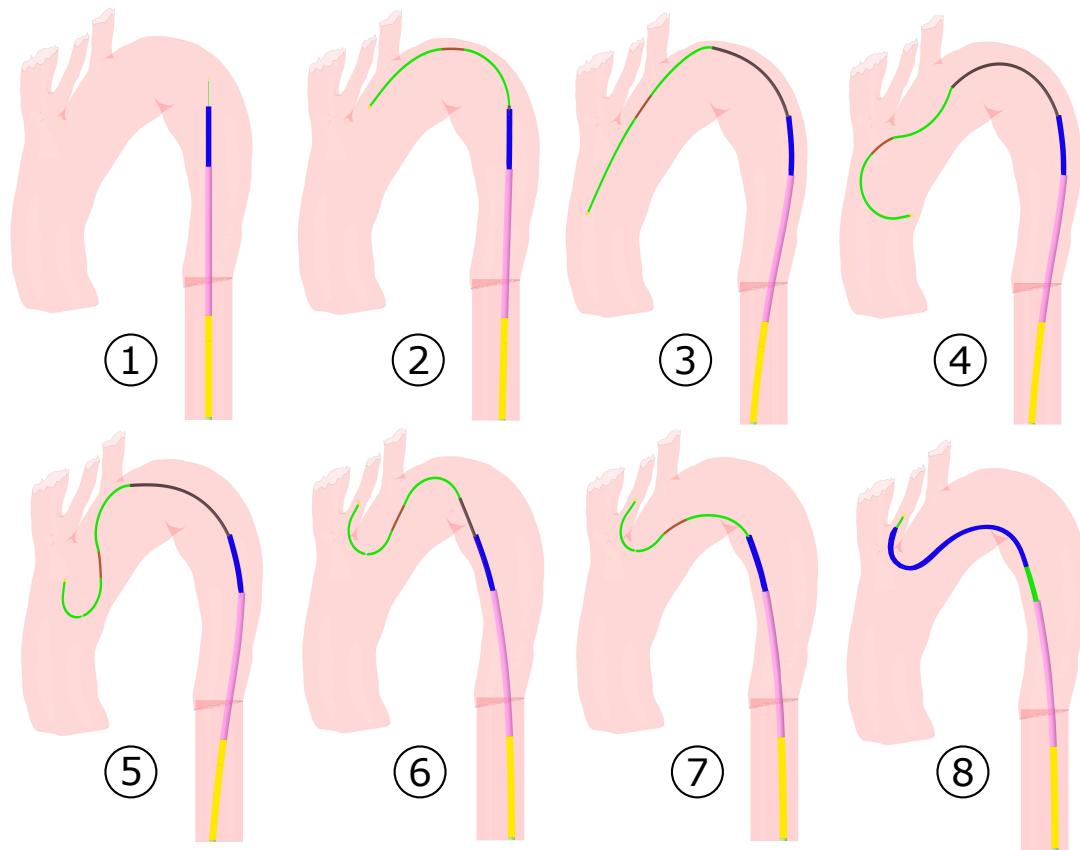


Figure 3: From ① to ③ the guidewire is initially pushed near the left carotid artery entrance. The two modules are activated in ④ while a rotation gesture is applied at the end of the active guidewire. As a consequence, the snapping effect appears(⑤) allowing to point the distal part of the guidewire in the desired direction and to stabilize the device. The guidewire is pulled from ⑥ to ⑦ to straighten the catheters with a deactivation of the proximal module to further tension it. Finally, the catheter slides over the guidewire until it reaches the left carotid artery in ⑧.

1.1.2.3 High fidelity simulations for the construction of decision support numerical charts

Two numerical charts are built for the endovascular navigation in two typical aortas: the BH aorta, which is referred to as a standard aorta, and the FM aorta, which includes a bovine arch (the left carotid artery and the brachio-cephalic trunk share the same origin). The key steps of active navigation into these aortas are illustrated Fig.4.

The distal modulus is systematically activated at the beginning of navigation to follow the shape of the arch and prevent the guidewire from entering the left subclavian artery. Therefore, the time of activation of the distal modulus is not a parameter. The output data recorded are the displacements of the guidewire distal part (73 mm blade) over time. The data are saved every 0.01s of the simulation over a total simulation time of 10.6 s and 11.5 s for the BH and FM aorta, respectively. Using two 2.30 GHz Xeon cores, the duration of a simulation is about 3 h.

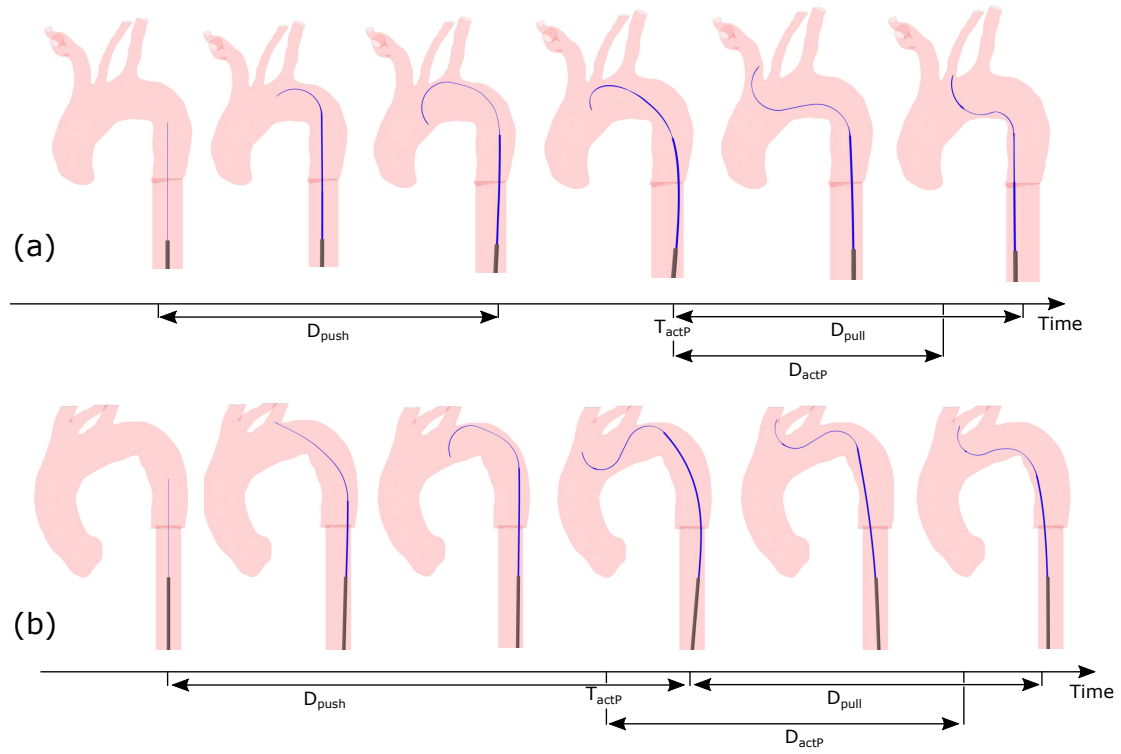


Figure 4: (a) Proposed navigation key steps for BH aorta hooking (standard aorta). The guidewire is pushed (during D_{push}) and the distal modulus is activated to prevent the device from inserting into the subclavian artery. After the guidewire is pushed, the proximal modulus is activated (at T_{actP} and during D_{actP}) and the snapping is initiated. The guidewire is then pulled (during D_{pull}). (b) The steps for navigation in the FM aorta (aorta with bovine arch) slightly differ: the guidewire navigates until it reaches the TSAs, the distal modulus is activated and snapping is triggered. The proximal modulus is then deactivated while pulling the guidewire to attempt to hook the carotid artery. Below each figure, navigation parameters driving the navigation are indicated on an axis representing time.

135 1.2 Development of numerical charts using reduced order modeling

136 Now that the high-fidelity FE models have been presented, the High Order Proper Generalized
 137 Decomposition (HOPGD) method used to build the numerical charts is presented. A focus is
 138 proposed on the choice of the parameters of interest in this work, as it is a critical step.

139 Then, two types of numerical charts are developed as proofs of concept: an active guidewire
 140 design tool focusing on design parameters and navigation assistance tools mixing design and
 141 navigation parameters. For each type of numerical chart, the parameter space and the snapshot
 142 selection method are presented. An error is finally calculated to evaluate the chart accuracy.

143 1.2.1 Methods

144 1.2.1.1 HOPGD

145 We consider a function u dependent on parameters $p_{i=1,d}$ which can be time, space or control
 146 parameters of the problem. These parameters are assimilated to extra-coordinates of the solution
 147 and discretized in the parameter space. For each set of parameters, HOPGD seeks an approximate
 148 form u^n of u such that:

$$u(p_1, \dots, p_d) \approx u^n(p_1, \dots, p_d) = \sum_{j=1}^n \prod_{i=1}^d F_i^j(p_i) \quad (3)$$

149 n is the order of approximation and the functions $F_{i=1,d}^j$ are related to the j -th mode. These
 150 functions are determined by solving the minimization problem which consists in finding
 151 $u^n \in V_n \subset \mathcal{L}^2(\Omega)$ minimizing the cost function J such that:

$$J(u^n) = \min_{u^n \in V_n} \left(\frac{1}{2} \|u^n - u\|_{\mathcal{L}^2(\Omega)}^2 \right) \quad (4)$$

152 This minimization problem can be solved by an alternating fixed point algorithm. For a new
 153 set of parameters, the new functions F_i are linearly interpolated from the existing functions. In
 154 this study, the version of the HOPGD algorithm does not use snapshot selection by *sparse grids*
 155 method as introduced in Lu et al. (2018). Thus, parameters discretization is conducted using
 156 uniform grids. Fig.5 illustrates the general procedure of the HOPGD method.

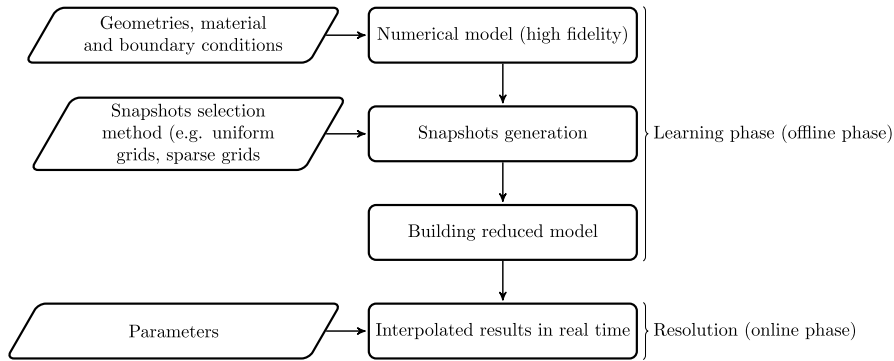


Figure 5: General procedure of the HOPGD method: starting from a high-fidelity numerical model, n parameters are considered among the geometry, material and boundary conditions. Then, the parameter space defined by the n axes is discretized using a snapshot selection method. For an uniform grid, m snapshots are selected along the axes forming a total of m^n snapshots. These snapshots are used to build the reduced model. Considering a new set of parameter within the parameter space, the HOPGD model is capable of providing a real-time response.

157 1.2.1.2 Error evaluation

158 In order to evaluate the numerical charts performance, so-called evaluation points are selected in
 159 the center of the subdomains of the snapshot grid in the parameter space.

160 For each of these evaluation points, an additional finite element calculation is performed and
 161 the displacements of guidewire distal part nodes are stored in a reference U^{ref} matrix, containing
 162 the so-called high fidelity results. The reduced model is used to interpolate the results on this
 163 point and the obtained displacements are in turn stored in a U matrix. For the considered point,

164 an error δ is computed such that:

$$\delta = \frac{\|U - U^{ref}\|}{\|U^{ref}\|} \quad (5)$$

165 With $\|\bullet\|$ the L_2 norm.

166 1.2.2 Application

167 Endovascular navigation involves many parameters. They can be classified into three categories:

168 (i) those related to the design of the active guidewire (e.g., lengths of the active moduli or
 169 distance between them), (ii) the parameters related to navigation such as activation times or
 170 pushing / pulling times of the surgical tools and (iii) those dealing with geometric parameters
 171 (patient-specific aortas). In our study, we decided to work with fixed geometry, i.e. the parameters
 172 only relate to the design of the active guidewire and those related to the clinician gestures
 173 during navigation. In the following, two types of numerical charts are presented. First, an active
 174 guidewire design aid tool with five control parameters that are related to the device design is
 175 presented. This tool allows to compute the performance of the activated guidewire for a given
 176 set of parameters. Then, considering the design and navigation parameters, decision support
 177 numerical charts are also proposed with seven control parameters.

178 1.2.2.1 Active guidewire design tool

179 This first tool aims to provide a design aid tool. From a given guidewire configuration, the tool
 180 computes in real time the deformation of the guidewire after activation of the moduli. The
 181 high-fidelity model used to generate the snapshots was presented in Section 1.1.1.3. The output of
 182 each snapshot corresponds to the distal guidewire position for a given design.

183 *Choice of parameters*

184 Five design parameters are selected for the development of the design support tool (Fig.6): the
 185 lengths L_p , L_d and e that are the lengths of the active moduli and the distance between them,
 186 respectively; parameters ϵ_L for the two Nitinol wires, which is the recoverable strain for the
 187 Nitinol wires in the shape memory effect loop representing the wire performances (change in
 188 current intensity or Nitinol grade for instance). Fig.6 also describes the parameter ranges.

189 *Snapshots selection*

190 As previously mentioned, the version of HOPGD we use in this work does not include the sparse
 191 grids method and therefore does not allow for optimal selection of snapshots in the parameter
 192 space. Thus, it is chosen for this numerical chart to build a uniform grid with a discretization of

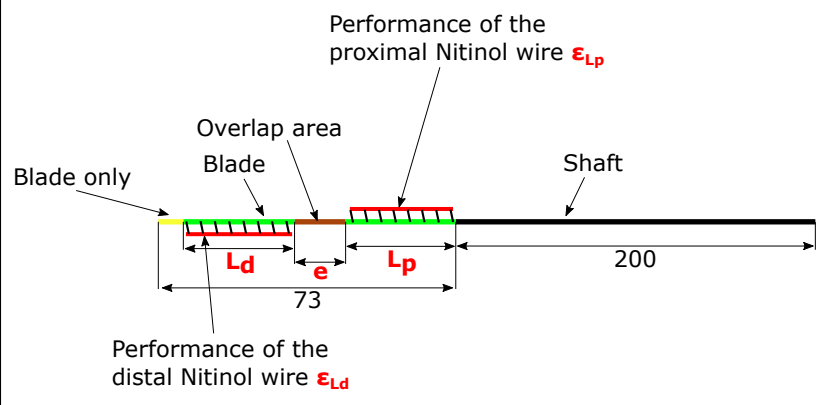
Model of the active guidewire highlighting the design parameters (bold red)	Parameters
	$L_p \in [15;20]$ (mm) $e \in [5;10]$ (mm) $L_d \in [15;40]$ (mm) $\epsilon_{L_p} \in [0.01;0.0347]$ $\epsilon_{L_d} \in [0.01;0.0347]$

Figure 6: Double stage guidewire activation model and design parameters ranges.

193 three values per parameter (extremal values and middle of each interval), yielding a grid of
 194 $3^5 = 243$ finite element calculations to feed the HOPGD method and create the reduced model. A
 195 MatLab (MathWorks, USA) routine is used to automatically create the snapshots with the design
 196 parameters as input data. Once the snapshots are computed, the HOPGD algorithm builds the
 197 reduced model with a default number of modes fixed at 20. The reduced model is then evaluated
 198 at the center of subdomains formed by the space parameter and using the error defined Section
 199 1.2.1.2.

200 1.2.2.2 Navigation assistance tools

201

202 *Introduction*

203 In this part, more sophisticated numerical charts are proposed taking into account both design
 204 and navigation parameters. These decision support tools compute the active navigation in a given
 205 anatomy for various sets of parameters. They are proofs of concept of decision support tools
 206 which could be used in the preoperative phase. Their main advantage is the real time response.
 207 The high-fidelity model used to generate the snapshots was presented in Section 1.1.2.3.

208 *Choice of parameters*

209 Among the design parameters, we focused on the distal active modulus, which plays a dominant
 210 role in active navigation. Thus, parameters L_d and ϵ_{L_d} are included (Fig.6). Only the performance
 211 of the NiTi wire given by ϵ_{L_p} is selected to drive the design of the proximal modulus (L_p fixed at
 212 27 mm and e at 13 mm).

213 The other four parameters drive navigation. From a preliminary sensitivity study, the choice
 214 is made to focus on the guidewire pushing and pulling time (D_{push} and D_{pull}) and the time and
 215 duration of the activation of the proximal modulus (noted T_{actP} and D_{actP} respectively). These

parameters are illustrated Fig.4. A MatLab routine was developed in this study to automatically generate the endovascular navigation models from selected parameters.

Table 1: Choice of the intervals for the seven parameters of the decision support charts. The intervals are given for the standard aorta case and with bovine arch.

Parameters	Range of values for the standard aorta / with bovine arch
L_d (mm)	[27 ; 32] / [27 ; 32]
ϵ_{L_p}	[0.026 ; 0.028] / [0.03 ; 0.033]
ϵ_{L_d}	[0.029 ; 0.033] / [0.033 ; 0.0347]
D_{push} (s)	[2.0 ; 3.5] / [4.2 ; 5.2]
D_{pull} (s)	[0.05 ; 1.5] / [1.7 ; 2.5]
T_{actP} (s)	[3.5 ; 4.5] / [4.7 ; 5.3]
D_{actP} (s)	[0.1 ; 0.6] / [1.8 ; 2.2]

Refinement and model accuracy

The accuracy of the navigation assistance tool is evaluated from an error defined, as explained in Section 1.2.1.2, as the difference between the high-fidelity model result and the reduced model result at the center of the hypercube defined by the parameter grid. However, we also propose here to dynamically improve the accuracy by adding a control loop (refinement) during the learning phase. The general procedure is visible in Fig.7.

For the construction of these numerical charts, the generation of a uniform grid similar to the one used for the design aid chart (3 values per parameter) would have required $3^7 = 2187$ snapshots. A method is therefore proposed to limit the generation of many snapshots while allowing the creation of charts with a satisfactory accuracy. Fig.8. shows an overview of the process considering a 2D parameter space.

This additional procedure allows to determine the axes to be refined (requiring the addition of snapshots at the axis centers) when the error at the center of the hypercube is greater than a threshold value (here 5%). Let us note P^i the i -th parameter for $i = 1, \dots, 7$, P_{max}^i the maximum value at parameter P^i (upper limit of the interval in Tab.1) and P_{middle}^i the middle of the interval of admissible values for the parameter P^i . Seven evaluation points, related to the seven parameters, are considered in order to determine which parameters most affect the error sensitivity. The first evaluation point corresponds to $\{P_{middle}^1, P_{max}^2, P_{max}^3, P_{max}^4, P_{max}^5, P_{max}^6, P_{max}^7\}$, evaluating the contribution of the first parameter. In the same way the second evaluation point corresponds to $\{P_{max}^1, P_{middle}^2, P_{max}^3, P_{max}^4, P_{max}^5, P_{max}^6, P_{max}^7\}$ and so on. The error as a function of time is then calculated for each of these evaluation points. The parameter axes associated with evaluation points whose maximum error exceeds 5% are refined by adding the midpoint on the parameter specific axis, for discretization of the snapshot grid. The procedure on a 2D case is illustrated

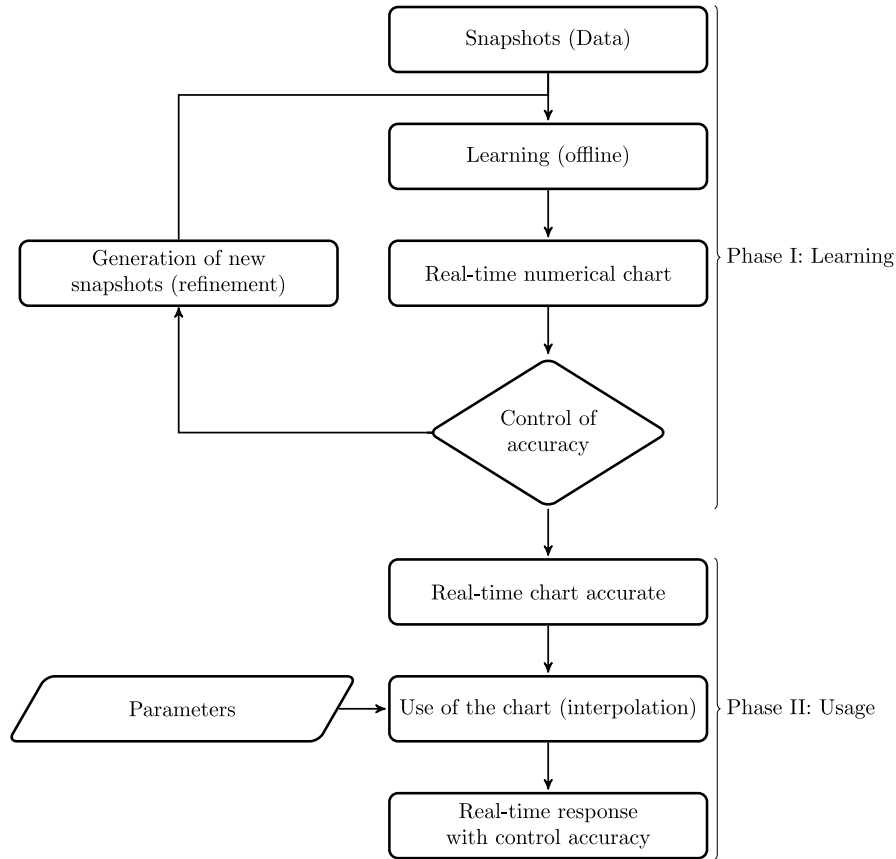


Figure 7: General procedure used for the development of decision support charts. From the snapshots computed in the parameter space in the learning phase, the reduced model is created and its accuracy is controlled. New snapshots are generated until the reduced model is considered as accurate enough. The real-time numerical chart is then used to give a real-time response given a set of parameters.

241 Fig.8.

242 In this part, we limit ourselves to a level 1 refinement (adding only one snapshot per direction)
 243 on three axes at most, which represents a final grid of $3^3 \times 2^3 = 432$ snapshots.

244 2 Results

245 2.1 Active guidewire design tool

246 From the 243 finite element snapshots, the reduced model is created by the HOPGD method
 247 in 17 seconds. The accuracy of the reduced model is evaluated at the different centers of the
 248 subdomains of the parameter space, i.e. on 32 evaluation points. The model is able to provide a
 249 solution in 10^{-5} s against 5 minutes for a FE calculation. The percentage errors at the different
 250 centers are given Tab.2. It is shown that the error is equal to or below 1%, which is satisfactory
 251 for accurately predicting the performance of a guidewire design.

252 The reduced model considerably decreases the computation time and allows to create the
 253 numerical chart visible on Fig.9. The graphical interface is developed with Qt Creator (Qt Group,
 254 Finland). The set of chosen parameters with the cursor interrogates the model and the interface

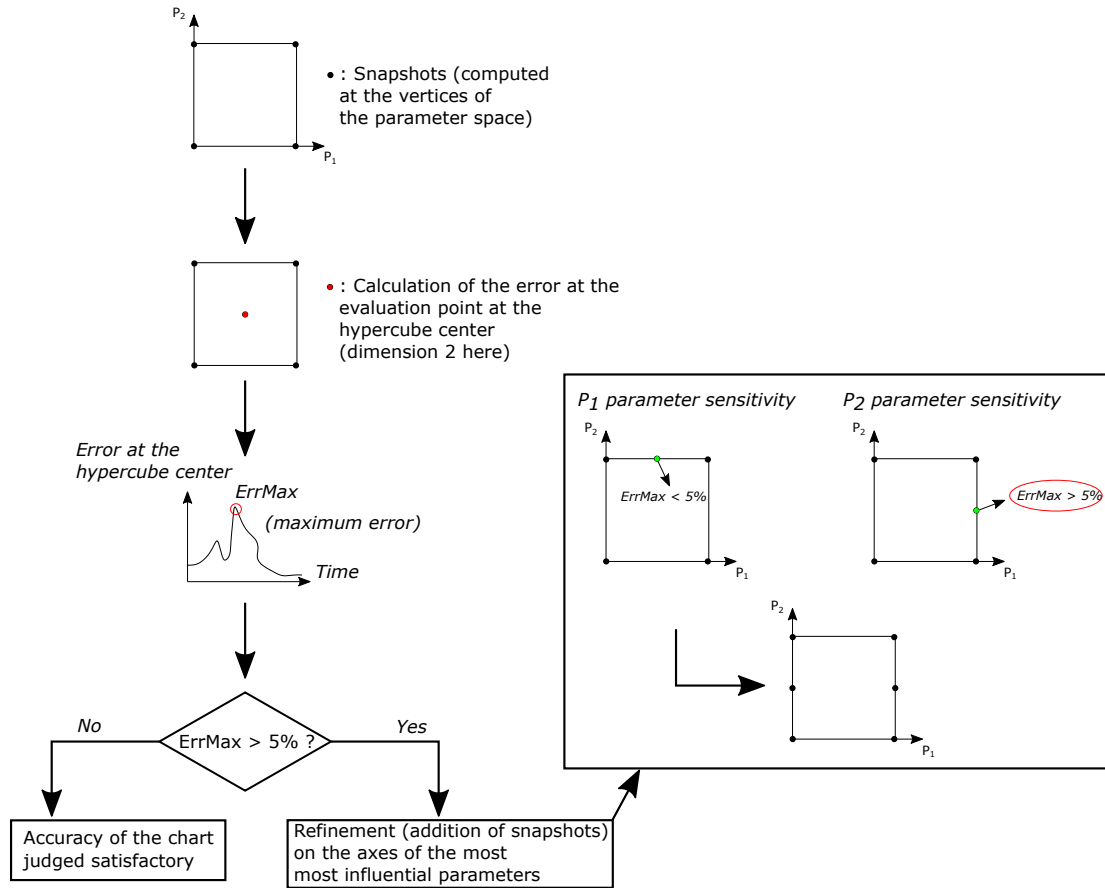


Figure 8: General procedure for the creation and refinement of decision support charts on typical aortas (learning phase in Fig.7). The first step is to perform the simulations on the parameter sets at the vertices of the grid. The error during navigation is then evaluated at the center of the hypercube. When this error exceeds a threshold fixed at 5%, the discretization in the parameter space is densified on the axes of the influential parameters (addition of snapshots at the center of these axes). Indeed, evaluation points (in green) are added at the middle of the parameter ranges to estimate sensitivity and errors are computed for both parameters. In the example, the error related to P_2 exceeds 5%. Consequently, the grid is refined to reduce the error at the hypercube center.

255 displays the corresponding guidewire displacements.

256 2.2 Navigation assistance tools

257 2.2.1 Standard aorta

258 From the snapshots at the grid vertices ($2^7 = 128$ snapshots), the reduced model is created in 77
 259 seconds. Using the method detailed in 1.2.2.2 to select the axes to be refined, values at the middle
 260 of the parameters axes of L_d , D_{pull} and T_{actP} are added, with a total number of snapshots at
 261 $3^3 \times 2^4 = 432$. The new model is built in 263 seconds and the error at the center of the hypercube
 262 is reduced. The performance, precision and parameters of the decision support tool developed are
 263 summarized in Fig.10.

264 2.2.2 Aorta with bovine arch

265 The procedure is similar for this chart applied to a bovine arch anatomy. The first model is built
 266 in 44 s but the error at the hypercube center required a refinement on the parameters axes of

Table 2: Errors at the center of the subdomains of the 5 control parameters for the design aid chart.

Subdomain number	Set of parameters	Error (in %)
1	{15.5; 5.5; 20.5; 0.016175; 0.016175}	0.79
2	{18.5; 5.5; 20.5; 0.016175; 0.016175}	0.85
3	{15.5; 8.5; 20.5; 0.016175; 0.016175}	0.78
4	{18.5; 8.5; 20.5; 0.016175; 0.016175}	0.77
5	{15.5; 5.5; 33.5; 0.016175; 0.016175}	0.72
6	{18.5; 5.5; 33.5; 0.016175; 0.016175}	0.91
7	{15.5; 8.5; 33.5; 0.016175; 0.016175}	0.9
8	{18.5; 8.5; 33.5; 0.016175; 0.016175}	0.88
9	{15.5; 5.5; 20.5; 0.028525; 0.016175}	1.00
10	{18.5; 5.5; 20.5; 0.028525; 0.016175}	0.96
11	{15.5; 8.5; 20.5; 0.028525; 0.016175}	0.82
12	{18.5; 8.5; 20.5; 0.028525; 0.016175}	0.73
13	{15.5; 5.5; 33.5; 0.028525; 0.016175}	0.90
14	{18.5; 5.5; 20.5; 0.028525; 0.016175}	1.01
15	{15.5; 8.5; 33.5; 0.028525; 0.016175}	0.91
16	{18.5; 8.5; 33.5; 0.028525; 0.016175}	0.92
17	{15.5; 5.5; 20.5; 0.016175; 0.028525}	0.85
18	{18.5; 5.5; 20.5; 0.016175; 0.028525}	0.90
19	{15.5; 8.5; 20.5; 0.016175; 0.028525}	0.79
20	{18.5; 8.5; 20.5; 0.016175; 0.028525}	0.79
21	{15.5; 5.5; 33.5; 0.016175; 0.028525}	0.56
22	{18.5; 5.5; 33.5; 0.016175; 0.028525}	0.70
23	{15.5; 8.5; 33.5; 0.016175; 0.028525}	0.67
24	{18.5; 8.5; 33.5; 0.016175; 0.028525}	0.77
25	{15.5; 5.5; 20.5; 0.028525; 0.028525}	0.91
26	{18.5; 5.5; 20.5; 0.028525; 0.028525}	0.98
27	{15.5; 8.5; 20.5; 0.028525; 0.028525}	0.86
28	{18.5; 8.5; 20.5; 0.028525; 0.028525}	0.83
29	{15.5; 5.5; 33.5; 0.028525; 0.028525}	0.68
30	{18.5; 5.5; 33.5; 0.028525; 0.028525}	0.81
31	{15.5; 8.5; 33.5; 0.028525; 0.028525}	0.78
32	{18.5; 8.5; 33.5; 0.028525; 0.028525}	0.81

²⁶⁷ D_{pull} and T_{actP} leading to a model created in 164 s based on $3^2 \times 2^5 = 288$ snapshots. The errors
²⁶⁸ of the model before and after refinement are displayed Fig.10 as well as the main characteristics
²⁶⁹ of this numerical chart. For the first numerical chart (standard aorta) a peak occurs at $t = 2$ s with
²⁷⁰ the distal module activation. At $t = 5$ s, snapping occurs and we can see that grid refinement
²⁷¹ highly improves the error with a better prediction of the position of the guidewire after snapping.
²⁷² For the second numerical chart, the error curves along time are fairly similar with a peak during
²⁷³ snapping. At $t = 8.5$ s, grid refinement allows to better describe the position of the guidewire
²⁷⁴ once pulled and the distal part abruptly hooked the aorta. The accuracy is considered satisfactory
²⁷⁵ considering the relatively low number of snapshots for such a problem.

²⁷⁶ 2.2.3 Conclusions on decision support charts

²⁷⁷ Overall, the charts show very satisfactory results. The snapping is correctly replayed and the
²⁷⁸ contact well represented. For each new set of parameters, the tools provide an instantaneous
²⁷⁹ response (10^{-3} s) compared to nearly 3 h for a high-fidelity FE calculation. The response time of

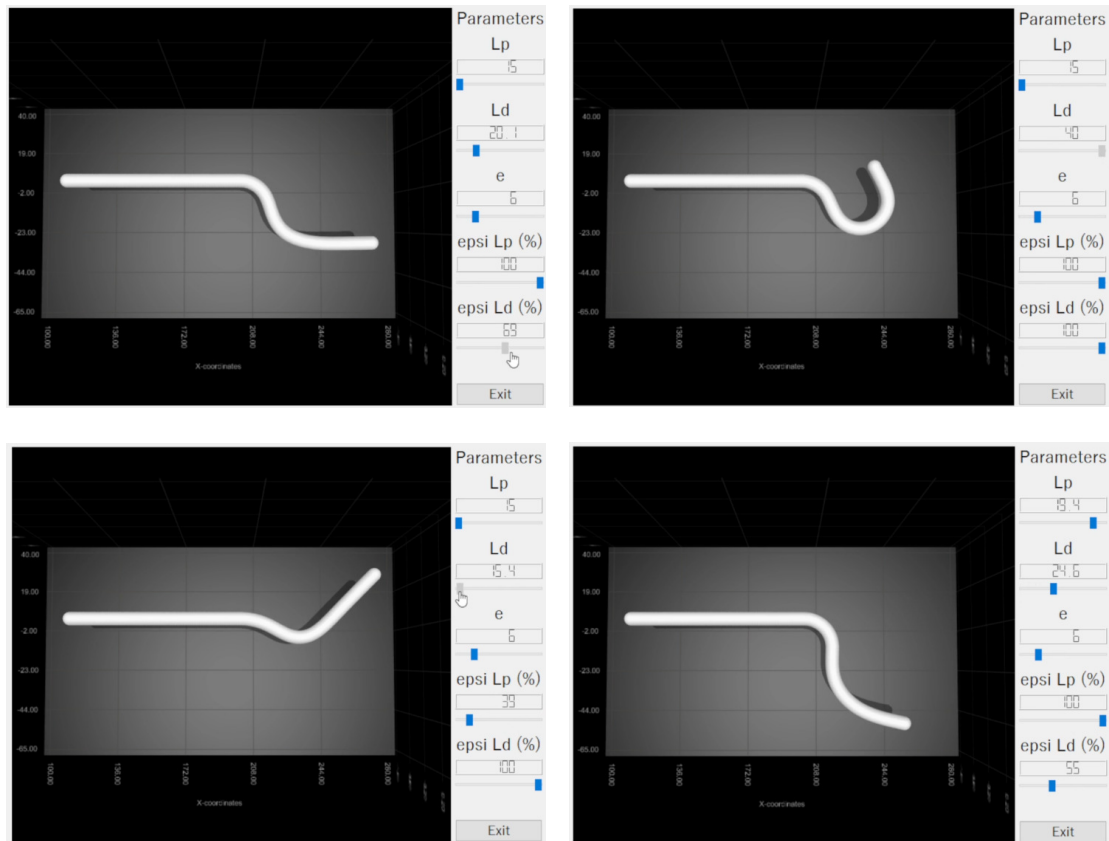


Figure 9: Numerical chart to help design the active guidewire. The five parameters can be modified and the tool allows to give a real time response of guidewire deformations with an accuracy of about 1%. A part of the rod is represented (left part of the rod) but has not been considered for the model construction. The figures represent different deformations of the guidewire according to the set of parameters defined by the user on the right panel.

280 the numerical chart is well below the specifications.

281 Concerning the error curves in blue for the two charts (Fig.10), peaks at key stages of the
 282 navigation are observed. The first peak occurs when the distal modulus is activated. While
 283 snapping, the error increases sharply. For the first chart, this error gradually decreases and then
 284 increases again when the guidewire is pulled. The second chart error curve shows successive
 285 peaks during snapping, mainly due to guidewire high frequency vibrations. A second peak is
 286 visible when the proximal modulus is deactivated.

287 3 Discussion

288 3.1 Main results

289 The HOPGD method was used to build numerical charts and proved to be efficient for problems
 290 with many parameters as it was the case in this study.

291 A first chart has been developed to help the guidewire design optimization. Only guidewire
 292 design parameters were studied. Considering the simulation time of the snapshots used to create
 293 the reduced model and the preliminary tests, it was chosen to work on a uniform grid with three

312 capture and control the fast movements of the tools. However it should be emphasized that this
313 chart provides the navigation over time and not only the final configuration. After refinement,
314 the error remains below 4% which can be considered as very satisfactory, especially because this
315 maximum error occurs at snapping. We expected this phenomenon to be much less reducible.
316 In general, it was interesting to test the performance of the HOPGD method in our problem
317 associating nonlinearities, contact and fast phenomena.

318 Recent research have been focusing on the development of Virtual Reality (VR) simulators to
319 join the growing expansion of endovascular techniques (Eves et al. 2022). While these efforts
320 aim at developing training and predictive platforms, the developed physical models remain
321 simple with general cases (not patient specific) and are mainly used to train novice practitioners
322 (Rudarakanchana et al. 2015). The goal of this paper is to provide perspectives on elaborating
323 high-fidelity numerical platforms to enhance VR tools, considering: (i) the inclusion of Finite
324 Element Method (FEM) in VR simulators, capable of accurately simulating passive and active tools,
325 and (ii) addressing the issue of patient-specificity through the use of deep learning techniques,
326 with Reduced Order Models (ROMs) or statistical shape analysis for instance (Iyer et al. 2023).

327 **3.2 Study limits**

328 Many tests (charts with less parameters, simulations to study the sensitivity to some parameters)
329 have been conducted beforehand and two main difficulties have been highlighted: the choice of
330 parameters and their range of values. The active guidewire was developed during this work. As a
331 consequence, there was not the necessary hindsight to choose, in an optimal way, the parameters
332 to be incorporated in the chart. We then relied on the experience gained from the numerous
333 simulations performed.

334 Concerning the values ranges, charts with two or three parameters allowed to show that too
335 large ranges would require many simulations. In order to develop proofs of concept and taking
336 into account the available resources, a maximum of 432 snapshots per chart was set. With seven
337 control parameters, the selected value intervals were therefore quite small and did not allow to
338 explore large variations of the guidewire navigation. The main limitation came from the use of
339 uniform grids. It would be interesting to improve the generation of snapshots with a sparse grid
340 method.

341 The errors for both decision support charts were evaluated at the center of the hypercube.
342 An error within 5% was considered satisfactory. This criterion was determined by judging
343 the displacements of the guidewire relative to the aorta: for the tested charts, a higher error
344 corresponded to poor management of the contact between the guidewire and the aorta. Moreover,

345 the peaks occurred during the fast phenomena: activation and deactivation of the modules or even
346 snapping. A solution to smoothen the curves could be to save more data as a function of time
347 (reduction of the time step used to save the guidewire displacements) so as to better capture these
348 phenomena. However, it would require a large amount of storage. A method, adapted specifically
349 for this study, allowed us to select the axes to refine the grid when this error exceeded 5%. For
350 intervals with larger extrema, further refinements in the sub-domains may be considered.

351 The HOPGD method relies on static parameters (scalar values), and recent developments
352 have been focusing on a dynamic ROM builder to better fit transient analysis and reduce the
353 number of learning points (Calka et al. 2021). However, the main difficulty associated with our
354 model is its sensitivity to parameters; even a slight change in them can significantly impact the
355 displacements of the guidewire. Thus, a dynamic ROM might also require a significant number of
356 points or further development to address these issues.

357 4 Conclusion

358 This study presents numerical charts for design and decision support tools dedicated to the use of
359 the active guidewire. These solutions serve as a proof of concept and show very promising
360 results. Fixed anatomy numerical charts were proposed in this study. A more powerful tool could
361 incorporate geometric parameters and allow, for a new patient, to provide real-time decision
362 support.

363 5 Backmatter information

364 **5.0.0.1 Acknowledgements** The French National Research Agency (ANR) partially supported
365 this work through the DEEP project: Devices for augmEnted Endovascular navigation in complex
366 Pathways (grant n°ANR-18-CE19-0027-01).

367 **5.0.0.2 Authors' contributions** A.B. carried out most of the study, performed numerical
368 simulations, and drafted the manuscript. A.D. helped with implementation of the methods. J.S.
369 and R.B. provided the clinical data. N.T. helped for the methodology and the experiments. N.H.
370 provided support for the numerical simulations. A.G. provided support for the model reduction
371 method and revised the article. A.B.B revised the article, contributed to the methodology and the
372 analysis of the results. All authors read and approved the final manuscript.

373 **5.0.0.3 Competing interests** The authors declare that there are no conflicts of interest.

374 **5.0.0.4 Open Access** This article is licensed under a Creative Commons Attribution 4.0
375 International License, which permits use, sharing, adaptation, distribution and reproduction in
376 any medium or format, as long as you give appropriate credit to the original author(s) and the
377 source, provide a link to the Creative Commons license, and indicate if changes were made. The
378 images or other third party material in this article are included in the article's Creative Commons
379 license, unless indicated otherwise in a credit line to the material. If material is not included in the
380 article's Creative Commons license and your intended use is not permitted by statutory regulation
381 or exceeds the permitted use, you will need to obtain permission directly from the copyright
382 holder. To view a full copy of this license, visit <http://creativecommons.org/licenses/by/4.0/>.

383 References

- 384 Badrou, A., N. Tardif, A. Even, P. Chaudet, N. Lescanne, J. Szewczyk, A. Gravouil, N. Hamila, and
385 A. Bel-Brunon (Oct. 2022). "Characterization of Surgical Tools for Specific Endovascular
386 Navigation". *Cardiovascular Engineering and Technology* 13.5, pp. 751–763. DOI: [10.1007/s13239-
387 022-00612-8](https://doi.org/10.1007/s13239-022-00612-8)
- 388 Badrou, A., N. Tardif, P. Chaudet, N. Lescanne, J. Szewczyk, R. Blanc, N. Hamila, A. Gravouil, and
389 A. Bel-Brunon (July 2022). "Simulation of multi-curve active catheterization for endovascular
390 navigation to complex targets". *Journal of Biomechanics* 140, p. 111147
- 391 Barone, A., M. G. Carlino, A. Gizzi, S. Perotto, and A. Veneziani (Dec. 2020). "Efficient estima-
392 tion of cardiac conductivities: A proper generalized decomposition approach". *Journal of
393 Computational Physics* 423, p. 109810
- 394 Calka, M., P. Perrier, J. Ohayon, C. Grivot-Boichon, M. Rochette, and Y. Payan (Jan. 2021). "Machine-
395 Learning based model order reduction of a biomechanical model of the human tongue".
396 *Computer Methods and Programs in Biomedicine* 198, p. 105786. DOI: [10.1016/j.cmpb.2020.105786](https://doi.org/10.1016/j.cmpb.2020.105786)
- 397 Couture, T. and J. Szewczyk (Nov. 2017). "Design and Experimental Validation of an Active
398 Catheter for Endovascular Navigation". *Journal of Medical Devices* 12
- 399 Darwish, A., G. Di Labbio, W. Saleh, and L. Kadem (June 2021). "Proper Orthogonal Decomposition
400 Analysis of the Flow Downstream of a Dysfunctional Bileaflet Mechanical Aortic Valve".
401 *Cardiovascular Engineering and Technology* 12.3, pp. 286–299
- 402 Eves, J., A. Sudarsanam, J. Shalhoub, and D. Amiras (Sept. 23, 2022). "Augmented Reality in
403 Vascular and Endovascular Surgery: Scoping Review". *JMIR Serious Games* 10.3, e34501. DOI:
404 [10.2196/34501](https://doi.org/10.2196/34501)

- 405 Herrmann, L. R. and F. E. Peterson (1968). “A Numerical Procedure for Viscoelastic Stress
406 Analysis”. Proc. 7th Meeting of ICRPG Mechanical Behavior Working Group. Orlando, FL.
- 407 Iyer, K., A. Morris, B. Zenger, K. Karanth, N. Khan, B. A. Orkild, O. Korshak, and S. Elhabian
408 (Jan. 12, 2023). “Statistical shape modeling of multi-organ anatomies with shared boundaries”.
409 *Frontiers in Bioengineering and Biotechnology* 10, p. 1078800. DOI: [10.3389/fbioe.2022.1078800](https://doi.org/10.3389/fbioe.2022.1078800)
- 410 Janiga, G. (Jan. 2019). “Quantitative assessment of 4D hemodynamics in cerebral aneurysms using
411 proper orthogonal decomposition”. *Journal of Biomechanics* 82, pp. 80–86
- 412 Kefayati, S. and T. L. Poepping (July 2013). “Transitional flow analysis in the carotid artery
413 bifurcation by proper orthogonal decomposition and particle image velocimetry”. *Medical
414 Engineering & Physics* 35.7, pp. 898–909
- 415 Lagoudas, D. C. (2008). *Introduction to shape memory alloys. In: Lagoudas DC (ed.) Shape Memory
416 Alloys. Vol. 1. Boston, MA: Springer US. pp.1–51*
- 417 Lu, Y., N. Blal, and A. Gravouil (2018a). “Adaptive sparse grid based HOPGD: Toward a nonintrusive
418 strategy for constructing space-time welding computational vademecum”. *International
419 Journal for Numerical Methods in Engineering* 114.13, pp. 1438–1461
- 420 Lu, Y., N. Blal, and A. Gravouil (2018b). “Multi-parametric space-time computational vademecum
421 for parametric studies: Application to real time welding simulations”. *Finite Elements in
422 Analysis and Design* 139, pp. 62–72
- 423 Madhwal, S., V. Rajagopal, D. Bhatt, C. Bajzer, P. Whitlow, and S. Kapadia (2008). “Predictors of
424 Difficult Carotid Stenting as Determined by Aortic Arch Angiography”. *J. Invasive. Cardiol.*
425 *20*, pp. 200–4
- 426 Modesto, D., S. Zlotnik, and A. Huerta (2015). “Proper generalized decomposition for parameterized
427 Helmholtz problems in heterogeneous and unbounded domains: Application to harbor
428 agitation”. *Computer Methods in Applied Mechanics and Engineering* 295, pp. 127–149
- 429 Niroomandi, S., D. González, I. Alfaro, F. Bordeu, A. Leygue, E. Cueto, and F. Chinesta (May 2013).
430 “Real-time simulation of biological soft tissues: a PGD approach”. *International Journal for
431 Numerical Methods in Biomedical Engineering* 29.5, pp. 586–600
- 432 Quesada, C., I. Alfaro, D. González, F. Chinesta, and E. Cueto (2018). “Haptic simulation of
433 tissue tearing during surgery”. *International Journal for Numerical Methods in Biomedical
434 Engineering* 34.3, e2926
- 435 Quesada, C., D. González, I. Alfaro, E. Cueto, and F. Chinesta (2016). “Computational vademecums
436 for real-time simulation of surgical cutting in haptic environments”. *International Journal for
437 Numerical Methods in Engineering* 108.10, pp. 1230–1247

- 438 Rama, R. R., S. Skatulla, and C. Sansour (Oct. 2016). “Real-time modelling of diastolic filling of the
439 heart using the proper orthogonal decomposition with interpolation”. *International Journal of*
440 *Solids and Structures* 96, pp. 409–422
- 441 Rudarakanchana, N., L. Desender, I. Van Herzeele, and N. J. Cheshire (Mar. 2015). “Virtual reality
442 simulation for the optimization of endovascular procedures: current perspectives”. *Vascular*
443 *Health and Risk Management*, p. 195. DOI: [10.2147/VHRM.S46194](https://doi.org/10.2147/VHRM.S46194)
- 444 Veith, F. J. (Oct. 2016). “A look at the future of vascular surgery”. *Journal of Vascular Surgery* 64.4,
445 pp. 885–890. DOI: [10.1016/j.jvs.2016.07.096](https://doi.org/10.1016/j.jvs.2016.07.096)